
Uncertainty-Aware Image Super-Resolution via Guided Diffusion

Anonymous Author(s)

Affiliation

Address

email

Abstract

Deep learning has recently attracted considerable attention from researchers in the natural sciences, particularly microscopists, for fast extraction of physically relevant information from images. In particular, single molecule localization microscopy has benefited significantly from recently developed deep kernel density estimators (KDE). However, simple and interpretable uncertainty quantification is lacking in these applications, and remains a necessary modeling component in high-risk research. In order to quantify uncertainty in otherwise deterministic image translation architectures, we propose a generative modeling framework based on denoising diffusion probabilistic models (DDPMs). Our model is inspired by guided diffusion, which condition the diffusion process with external cues or their derivatives. We propose uncertainty estimation by using a guided diffusion process to target diffusion toward a space of reasonable solutions through conditioning the score-estimator on a strong initial guess. This approach allows us to probe the structure of the distribution on reconstructions and estimate uncertainties. Our model is tested on KDE estimation in fluorescence microscopy, and we demonstrate that blending the traditional architectures with a DDPM permits simultaneous high-fidelity super-resolution with uncertainty estimation of regressed KDEs.

1 Introduction

Deep learning has attracted tremendous attention from researchers in the natural sciences, with several foundational applications arising in microscopy, e.g., (Weigert 2018; Falk 2019). Recently, the application of deep image translation in single-molecule localization microscopy (SMLM) has received considerable interest (Ouyang 2018; Nehme 2020; Speiser 2021). SMLM techniques are a mainstay of fluorescence microscopy and can be used to produce a pointillist representation of biomolecules in the cell at diffraction-unlimited precision (Rust 2006; Betzig 2006). In previous applications of deep models to localization microscopy, super-resolution images can be recovered from a sparse set of localizations with conditional generative adversarial networks (Ouyang 2018) or kernel density estimation can be performed using traditional convolutional networks (Nehme 2020; Speiser 2021). Here, we focus on the latter class of models which perform KDE estimation using neural networks.

Inferences in SMLM, and other super-resolution image reconstruction tasks, are often made on a single measurement, and thus common measures of model performance are based on localization errors computed over ensembles of simulated images. Unfortunately, this choice precludes computation of uncertainty at test time under a fixed model. Yet, Bayesian probability theory offers us mathematically grounded tools to reason about model uncertainty, but these usually come with a prohibitive computational cost (Gal 2022). A few approaches to avoiding this intractability in deep models have been deterministic uncertainty quantification (Amersfoort 2020), ensembling (Lakshminarayanan et al., 2017) or Monte Carlo dropout (Gal and Ghahramani, 2016). Here, we choose to



Figure 1: Generative model of single molecule localization microscopy images

model a distribution on high-resolution KDE predictions conditioned on a low-resolution input using a denoising diffusion probabilistic model (DDPM) (Ho 2020; Song 2021). Such models are one class of *score based generative models* which implicitly compute the score of the data distribution at each noise scale starting from pure noise (Song 2021). This approach has proven powerful for generative modeling of conditional image distributions; however, conditional diffusion can become trapped in local optima preventing the application of such models to uncertainty estimation.

In statistical physics, particularly simulation of complex molecular systems, sampling is constrained to a limited set of configurations. For this reason, sampling begins at a presumed global optimum, which is typically a configuration with minimal energy (Levitt 1983). Similar notions of constrained diffusion have been used in DDPMs to guide the process based on gradients of a classifier (Nichols 2021). Importantly, in the context of DDPMs, the forward process is ill defined for corruption of a target image to a estimated global optimum. We therefore propose a guided diffusion process which targets diffusion toward a space of reasonable solutions by conditioning the score-estimator on a strong initial guess. This approach allows us to probe the structure of the distribution of reconstructions, with fewer iterations than standard diffusion models. Indeed, the entropy of estimated reconstructions obtained from guided diffusion must upper bound the entropy of reconstructions obtained from low-resolution inputs. This technique could be readily integrated with existing localization performance measures to address both model accuracy on training data and precision on datasets produced by experiments.

2 Background

2.1 Image Likelihood and Localization Error

The central objective of single molecule localization microscopy is to infer a set of molecular coordinates θ from measured low resolution images \mathbf{x} . The likelihood on a particular pixel k , i.e., $p(\mathbf{x}_k|\theta)$ is taken to be a convolution of Poisson and Gaussian distributions, due to shot noise $p(s_k) = \text{Poisson}(\omega_k)$ and sensor readout noise $p(\zeta_k) = \mathcal{N}(o_k, \sigma_k^2)$

$$p(\mathbf{x}_k|\theta) = A \sum_{q=0}^{\infty} \frac{1}{q!} e^{-\omega_k} \omega_k^q \frac{1}{\sqrt{2\pi}\sigma_k} e^{-\frac{(\mathbf{x}_k - g_k q - o_k)^2}{2\sigma_k^2}} \approx \text{Poisson}(\omega'_k) \quad (1)$$

where A is some normalization constant and $\omega'_k = \omega_k + \sigma_k^2$. For the sake of generality, we include a per-pixel gain factor g_k , which is often unity. In practice, the summation in (1) can be difficult to work with, and it is common to instead use a Poisson-Normal approximation for simplification, valid under a range of experimental conditions (Huang 2013). This result can be seen from the fact the the convolution of two Poisson distributions is also Poisson. The expectation of the Poisson process at each pixel of the image is computed from the optical transfer function $O(u, v)$, which is often a two-dimensional isotropic Gaussian.

$$\omega = i_0 \iint O(u, v) du dv \quad (2)$$

The above integration can be carried out by computing differences of error functions, as detailed in Appendix A. The complete generative process is depicted in Figure 1.

Reliable estimation of θ from \mathbf{x} , for example by maximum likelihood estimation or with a deep model, requires performance metrics for model selection. We use the Fisher information as an information theoretic criteria to assess the quality of the model tested here, with respect to the root mean squared error (RMSE) of our predictions of θ (Chao 2016). The Poisson log-likelihood $\ell(\mathbf{x}|\theta)$ is also convenient for computing the Fisher information matrix (Smith 2010) and thus the Cramer-Rao lower bound, which bounds the variance of a statistical estimator of θ , from below i.e., $\text{var}(\hat{\theta}) \geq I^{-1}(\theta)$. The Fisher information is straightforward to compute under the Poisson log-likelihood, which is detailed in the Appendix

$$\mathcal{I}_{ij}(\theta) = \mathbb{E}_{\theta} \left(\frac{\partial \ell}{\partial \theta_i} \frac{\partial \ell}{\partial \theta_j} \right) = \sum_k \frac{1}{\omega'_k} \frac{\partial \omega'_k}{\partial \theta_i} \frac{\partial \omega'_k}{\partial \theta_j} \quad (3)$$

2.2 Kernel density estimation with deep networks

Direct optimization of the likelihood in (1) from observations \mathbf{x} alone is challenging when fluorescent emitters are dense within the field of view and fluorescent signals significantly overlap. However, convolutional neural networks (CNN) have recently proven to be powerful tools fluorescence microscopy to extract parameters describing fluorescent emitters such as color, emitter orientation, z -coordinate, and background signal (Zhang 2018; Kim 2019; Zelger 2018). For localization tasks, CNNs typically employ upsampling layers to reconstruct Bernoulli probabilities of emitter occupancy (Speiser 2021) or kernel density estimates with higher resolution than experimental measurements (Nehme 2020). We choose to use kernel density estimates in our model, denoted by \mathbf{y} . KDEs are the most common data structure used in SMLM, and can be easily generated from molecular coordinates, alongside observations \mathbf{x} , using well-understood models of the optical impulse response (Zhang 2007).

3 Image Super-Resolution via Guided Diffusion

We consider datasets $(\mathbf{x}_i, \mathbf{y}_i, \hat{\mathbf{y}}_i)_{i=1}^N$ of observed images \mathbf{x}_i true kernel density estimate (KDE) images \mathbf{y}_i , and KDE estimates $\hat{\mathbf{y}}_i = \phi(\mathbf{x}_i)$. Observations \mathbf{x}_i are simulated under the Poisson likelihood (1) and KDEs are generated using (2) alone, followed by appropriate normalization.

3.1 Problem Statement

Point estimates $\hat{\mathbf{y}}_i$ produced by the traditional deep architectures for super resolution microscopy produce strong results, but lack uncertainty quantification. Recent advances in generative modeling, particularly DDPMs, therefore present a unique opportunity to integrate uncertainty awareness into the super-resolution microscopy toolkit. However, sampling from DDPMs is computationally expensive, given that generation amounts to solving a complex stochastic differential equation, effectively mapping a simple base distribution to the complex data distribution. The solution of such equations requires numerical integration with very small step sizes, resulting in thousands of neural network evaluations (Saharia 2021; Vahdat 2021). Furthermore, for conditional generation tasks in high-risk applications, generation complexity is further exacerbated by the need for the highest level of detail in generated samples.

Certain conditional generation tasks, like sampling high-resolution images given low-resolution inputs, modeling the posterior is far more important than diversity in generated samples. Therefore, we propose that DDPM sampling is preceded by a deterministic neural network ϕ , which effectively seeds sampling in a target mode. Reasoning for this choice in our application is two-fold:

Synthesis Speed. By training a preprocessor ϕ to obtain an approximate estimate of \mathbf{y} , we can reduce the number of iterations, since the DDPM only needs to model the remaining mismatch, resulting in a less complex model from which sampling becomes easier. Speed is critical in SMLM applications, which can produce large volumes of image data in a single experiment.

Sample Fidelity. Since Langevin dynamics will often be initialized in low-density regions of the data distribution, inaccurate score estimation in these regions will negatively affect the sampling process (Song 2019). Moreover, mixing can be difficult because of the need of traversing low density regions

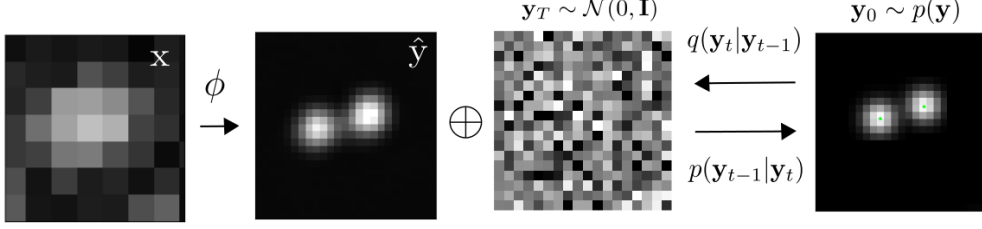


Figure 2: Conditional diffusion model for sampling kernel density estimates

118 to transition between modes of the distribution. Preprocessing with a deterministic mapping ϕ can
 119 ameliorate this issue, by eliminating the need for score estimation in low density regions.

120 Here, the preprocessor ϕ is realized by a CNN with upsampling layers. Consider the Markov chain
 121 wherein the KDE \mathbf{y} is latent in and inferred from a noisy measurement \mathbf{x} , i.e., $\mathbf{x} \rightarrow \phi(\mathbf{x}) \rightarrow \hat{\mathbf{y}}$. By
 122 the data processing inequality the function ϕ can only destroy information in \mathbf{x} pertaining to \mathbf{y} i.e.,
 123 $I(\mathbf{x}; \mathbf{y}) \geq I(\phi(\mathbf{x}); \mathbf{y})$ or $h(\mathbf{y}|\phi(\mathbf{x})) \geq h(\mathbf{y}|\mathbf{x})$ where I is the mutual information and h is the entropy.
 124 This suggests that the uncertainty in $p_\Psi(\mathbf{y}|\phi(\mathbf{x}))$ is indeed an upper bound on the entropy of $p(\mathbf{y}|\mathbf{x})$.

125 In practice, a DDPM Ψ can be trained on pairs $(\mathbf{y}_i, \hat{\mathbf{y}}_i)_{i=1}^N$. The conditional DDPM generates a target
 126 KDE \mathbf{y}_0 in T refinement steps. Starting with a pure noise image $\mathbf{y}_T \sim \mathcal{N}(0, \mathbf{I})$, the model iteratively
 127 refines the KDE through successive iterations according to learned conditional transition distributions
 128 $p(\mathbf{y}_{t-1}|\mathbf{y}_t)$ such that $\mathbf{y}_0 \sim p(\mathbf{y}|\hat{\mathbf{y}})$

129 3.2 Guided Diffusion

130 Diffusion models (Sohl-Dickstein 2015; Ho 2020; Song 2021) are a class of generative models
 131 inspired by nonequilibrium statistical physics, which slowly destroy structure in a data distribution
 132 $p(\mathbf{y}_0|\mathbf{x})$ via a fixed Markov chain referred to as the *forward process*. In the present context, we
 133 apply leverage recent results from (Ho 2020; Song 2021; Saharia 2021) for applying this framework
 134 to sampling from $p(\mathbf{y}|\mathbf{x}, \hat{\mathbf{y}})$. The forward process gradually adds Gaussian noise to the KDE \mathbf{y}
 135 according to a variance schedule $\beta_{0:T}$

$$q(\mathbf{y}_t|\mathbf{y}_0) = \prod_{t=1}^T q(\mathbf{y}_t|\mathbf{y}_{t-1}) \quad q(\mathbf{y}_t|\mathbf{y}_{t-1}) = \mathcal{N}\left(\sqrt{1 - \beta_t}\mathbf{y}_{t-1}, \beta_t \mathbf{I}\right) \quad (4)$$

136 The usual procedure is then to learn a parametric representation of the *reverse process*, and therefore
 137 generate samples from $p(\mathbf{y}_0)$, starting from noise. Formally, $p_\theta(\mathbf{y}_0|\hat{\mathbf{y}}) = \int p_\theta(\mathbf{y}_{0:T}|\hat{\mathbf{y}}) d\hat{\mathbf{y}}_{1:T}$ where
 138 \mathbf{y}_t is a latent representation with the same dimensionality of the data. $p_\theta(\mathbf{y}_{0:T}|\hat{\mathbf{y}})$ is a Markov process,
 139 starting from a noise sample $p_\theta(\mathbf{y}_T) = \mathcal{N}(0, \mathbf{I})$.

$$p_\theta(\mathbf{y}_{0:T}) = p_\theta(\mathbf{y}_T) \prod_{t=1}^T p_\theta(\mathbf{y}_{t-1}|\mathbf{y}_t) \quad p_\theta(\mathbf{y}_{t-1}|\mathbf{y}_t) = \mathcal{N}(s_\theta(\mathbf{y}_t), \beta_t \mathbf{I}) \quad (5)$$

140 where we reuse the variance schedule of the forward process (Ho 2020). We omit conditioning
 141 on $\hat{\mathbf{y}}$ for each transition density $p_\theta(\mathbf{y}_{t-1}|\mathbf{y}_t)$, as this is only considered at $t = 0$ i.e., $p_\theta(\mathbf{y}_1|\mathbf{y}_0, \hat{\mathbf{y}})$.
 142 An important property of the forward process is that it admits sampling \mathbf{y}_t at an arbitrary timestep
 143 t in closed form (Ho 2020). Using the notation $\alpha_t := 1 - \beta_t$ and $\gamma_t := \prod_{s=1}^t \alpha_s$, we have
 144 $q(\mathbf{y}_t|\mathbf{y}_0) = \mathcal{N}(\sqrt{\gamma_t}\mathbf{y}_0, (1 - \gamma_t)\mathbf{I})$.

$$\mathcal{L}(\theta) = \mathbb{E}[-\log p_\theta(\mathbf{y}_0|\mathbf{x})] \leq \mathbb{E}\left[-\log \frac{p_\theta(\mathbf{y}_{0:T}|\mathbf{x})}{q(\mathbf{y}_{1:T}|\mathbf{y}_0)}\right] \quad (6)$$

145 The objective in (6) can be expanded in terms of $D_{\text{KL}}(p(\mathbf{y}_{t-1}|\mathbf{y}_t)||q(\mathbf{y}_t|\mathbf{y}_{t-1}))$ as detailed in (Ho
 146 2020). We choose to adopt the simplified form of the variational bound, which emphasizes that the
 147 DDPM estimates the score $\nabla_{\mathbf{y}} \log p(\mathbf{y}|\mathbf{x})$ at each noise level (Song 2021)

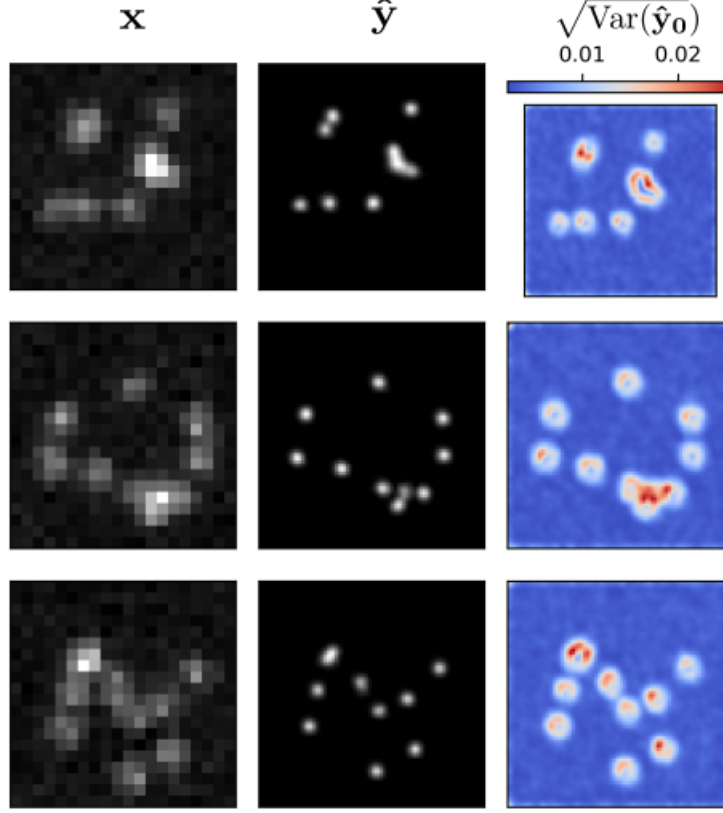


Figure 3: Kernel density estimates for various signal to noise ratios (SNR)

$$\theta^* = \underset{\theta}{\operatorname{argmin}} \mathbb{E}_{(\hat{\mathbf{y}}, \mathbf{y}_0) \in (\epsilon, \gamma)} \mathbb{E} \left[s_{\theta} \left(x, \sqrt{\gamma} \mathbf{y}_0 + \sqrt{1 - \gamma} \epsilon \middle| \mathbf{y}_t, \gamma \right) - \epsilon \right], \quad (7)$$

148 After training, samples can be generated by

$$\mathbf{y}_{t-1} = \frac{1}{\sqrt{1 - \beta_i}} (\mathbf{y}_i + \beta_i s_{\theta}(\mathbf{y}_t)) + \sqrt{\beta_i} \xi \quad (8)$$

149 For many conditional generation tasks, estimation of the gradient s_{θ} in low-density regions in order
 150 to drive (8) toward high-density regions is unnecessary and reduces performance of the sampler. Here,
 151 we instead propose an “energy-minimization” procedure preceding Langevin-based sampling in a
 152 DDPM, in order to speed up sampling from the equilibrium distribution

$$\hat{\mathbf{y}} = \underset{\mathbf{y}}{\operatorname{argmin}} \|\mathbf{y} - \mathbf{y}_0\|^2 \quad (9)$$

153 4 Experiments

154 All training data consists of low-resolution 20×20 images, simulated under the likelihood and impulse
 155 response (2,10), setting $\sigma = 0.92$ low-resolution pixels, for consistency with common experimental
 156 conditions with a 60X magnification objective lens and numerical aperture (NA) of 1.4. We choose
 157 $\omega_k = 200$ for experiments for consistency with typical bright fluorophore emission rates. All KDEs
 158 have dimension 80×80 , are scaled between $[0, 1]$, and are generated using $\sigma = 3.0$ pixels in the
 159 upsampled image. For a typical CMOS camera, this results in KDE pixels with lateral dimension of
 160 $\approx 27\text{nm}$. Initial coordinates θ were drawn uniformly over a two-dimensional disc with a radius of 7
 161 low-resolution pixels.

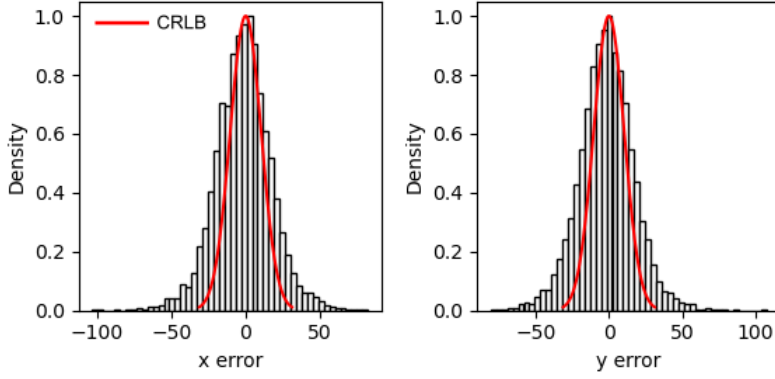


Figure 4: Localization errors of the trained model

162 4.1 Localization RMSE

163 In order to verify the initial predictions made by the model ϕ , we simulated a dataset $(\mathbf{x}_i, \mathbf{y}_i, \hat{\mathbf{y}}_i)_{i=1}^N$
 164 with $N = 1000$, and detect objects in the predicted KDE, $\hat{\mathbf{y}}_i$ using the Laplacian of Gaussian (LoG)
 165 detection algorithm (Lindeberg 2013). For simplicity, the localization is carried out from scale-space
 166 maxima directly in LoG, as opposed to fitting a model function to KDE predictions. A particular
 167 LoG localization in the KDE is paired to the nearest ground truth localization and is unpaired if a
 168 localization is not within 5 KDE pixels of any ground truth localization. In addition to localization
 169 error, we measured a precision $P = TP / (TP + FP) = 1.0$ and recall $R = TP / (TP + FN) = 0.85$,
 170 where TP denotes true positive localizations, FP denotes false positive localizations, and FN denotes
 171 false negative localizations.

172 4.2 Guided Diffusion

173 We set $T = 100$ for all experiments and treat forward process variances β_t as hyperparameters,
 174 with a linear schedule from $\beta_0 = 10^{-4}$ to $\beta_T = 10^{-2}$. These constants were chosen to be small
 175 relative to ground truth KDEs, which are scaled to $[-1, 1]$, ensuring that forward process distribution
 176 $\mathbf{y}_T \sim q(\mathbf{y}_T | \mathbf{y}_0)$ approximately matches the reverse process $\mathbf{y}_T \sim \mathcal{N}(0, I)$ at $t = T$.

177 To represent the reverse process, we used a DDPM architecture based on a U-Net backbone proposed
 178 in (Saharia 2021). We chose a U-Net backbone with channel multipliers $[1, 2, 4, 8, 8]$ in the downsam-
 179 pling and upsampling paths of the architecture. Parameters are shared across time, which is specified
 180 to the network using the Transformer sinusoidal position embedding. We use self-attention at the
 181 16×16 feature map resolution. To condition the model on the input $\hat{\mathbf{y}}$, we concatenate the $\hat{\mathbf{y}}$ estimated
 182 by DeepSTORM along the channel dimension, which are scaled to $[0, 1]$, with $\mathbf{y}_T \sim \mathcal{N}(0, I)$. Others
 183 have experimented with more sophisticated methods of conditioning, but found that the simple
 184 concatenation yielded similar generation quality (Saharia 2021).

185 5 Conclusion

186 References

- 187 [1] Nehme, E., et al. *DeepSTORM3D: dense 3D localization microscopy and PSF design by deep learning*.
 188 Nature Methods 17, 734–740 (2020).
- 189 [2] Ouyang, W., et al. *Deep learning massively accelerates super-resolution localization microscopy*. Nature
 190 Biotechnology 36, 460–468 (2018).
- 191 [3] Speiser, A., et al. *Deep learning enables fast and dense single-molecule localization with high accuracy*.
 192 Nature Methods 18, 1082–1090 (2021).
- 193 [4] Sohl-Dickstein J., et al. *Deep unsupervised learning using nonequilibrium thermodynamics*. ICLR (2015).

194 [5] Ho J., et al. *Denoising Diffusion Probabilistic Models*. Advances in Neural Information Processing Systems
195 (2015).

196 [6] Nanxin C., et al. *WaveGrad: Estimating Gradients for Waveform Generation*. ICLR (2021).

197 [4] Chao, J., et al. *Fisher information theory for parameter estimation in single molecule microscopy: tutorial*.
198 Journal of the Optical Society of America A 33, B36 (2016).

199 [5] Schermelleh, L. et al. *Super-resolution microscopy demystified*. Nature Cell Biology vol. 21 72–84 (2019).

200 [6] Zhang, B., et al. *Gaussian approximations of fluorescence microscope point-spread function models*. (2007).

201 [7] Smith, C.S., *Fast, single-molecule localization that achieves theoretically minimum uncertainty*. Nature
202 Methods 7, 373–375 (2010).

203 [8] Nieuwenhuizen, R., et al. *Measuring image resolution in optical nanoscopy*. Nature Methods 10, 557–562
204 (2013).

205 [9] Huang, F., et al. *Video-rate nanoscopy using sCMOS camera-specific single-molecule localization algorithms*.
206 Nat Methods 10, 653–658 (2013).

207 [10] Rust, M., et al. *Sub-diffraction-limit imaging by stochastic optical reconstruction microscopy (STORM)*.
208 Nat Methods 3, 793–796 (2006).

209 [11] Betzig, E., et al. *Imaging intracellular fluorescent proteins at nanometer resolution*. Science 313, 1642–1645
210 (2006).

211 [12] Weigert, M., et al. *Content-aware image restoration: pushing the limits of fluorescence microscopy*. Nat.
212 Methods 15, 1090 (2018).

213 [13] Falk, T., et al. *U-net: deep learning for cell counting, detection, and morphometry*. Nat. Methods 16, 67–70
214 (2019).

215 [14] Boyd, N., et al. *DeepLoco: fast 3D localization microscopy using neural networks*. Preprint at bioRxiv
216 <https://doi.org/10.1101/267096> (2018)

217 [15] Zelger, P., et al. *Three-dimensional localization microscopy using deep learning*. Opt. Express 26,
218 33166–33179 (2018)

219 [16] Zhang, P., et al. *Analyzing complex single-molecule emission patterns with deep learning*. Nat. Methods 15,
220 913 (2018)

221 [17] Saharia, C., et al. *Image Super-Resolution via Iterative Refinement*. Preprint at arXiv
222 <https://doi.org/10.48550/arXiv.2104.07636> (2021)

223 [18] Kim, T., et al. *Information-rich localization microscopy through machine learning*. Nat Commun 10, 1996
224 (2019).

225 A Appendix

226 Standard SMLM localization algorithms based on maximum likelihood estimators or least squares
227 optimization require tight control of activation and reactivation to maintain sparse emitters, presenting
228 a tradeoff between imaging speed and labeling density. Recently, deep models have generalized
229 SMLM to densely labeled structures by predicting high-resolution kernel density estimates (KDEs)
230 from low resolution images with convolutional networks. However, estimated KDEs may contain
231 irregularities due to finite sample sizes and limited model capacity.

232 The DeepSTORM CNN, initially proposed in (Nehme 2020) for 3D localization, can be viewed
233 as a deep kernel density estimator, reconstructing kernel density estimates \mathbf{y} from low-resolution
234 inputs \mathbf{x} . We utilize a simplified form of the original architecture for 2D localization, which we
235 denote ϕ hereafter, which consists of three main modules: a multi-scale context aggregation module,
236 an upsampling module, and a prediction module. For context aggregation, the architecture utilizes
237 dilated convolutions to increase the receptive field of each layer. The upsampling module is then
238 composed of two consecutive 2x resize-convolutions, computed by nearest-neighbor interpolation,
239 to increase the lateral resolution by a factor of 4. For a common sCMOS camera, each pixel has a
240 lateral size of approximately 108 nanometers, giving approximately 27 nanometer pixels in the KDE.
241 The terminal prediction module contains three additional convolutional blocks for refinement of the
242 upsampled image, followed by an element-wise HardTanh.

Single molecule localization microscopy (SMLM) relies on the temporal resolution of fluorophores whose spatially overlapping point spread functions would otherwise render them unresolvable at the detector. Common strategies for the temporal separation of molecules involve molecular photoswitching from dark to fluorescent states, permitting resolution of fluorophores beyond the diffraction limit. Estimation of molecular coordinates is typically carried out by modeling the optical impulse response of the imaging system and fitting model functions to the data. However, such models are only well-suited to isolated molecules, reducing the number of molecules in the field of view and limiting temporal resolution in super resolution microscopy. This issue has incited a series of efforts to increase the density of fluorescent molecules imaged in a single frame while developing appropriate models for dense localization.

In fluorescence microscopy, each pixel is treated as a Poisson random variable (Smith 2010; Nehme 2020; Chao 2016), with expected value

$$\omega = i_0 \int O(u) du \int O(v) dv \quad (10)$$

where $i_0 = \eta N_0 \Delta$. The scalar parameters η, Δ are the photon detection probability of the sensor and the exposure time, respectively. Without loss of generality, we assume $\eta = \Delta = 1$. Most importantly, N_0 represents the signal amplitude, which we assume maintains a fixed value. The optical impulse response $O(u, v)$ is often approximated as a 2D isotropic Gaussian with standard deviation σ (Zhang 2007). This approximation has the convenient property, that the effects of pixelation can be expressed in terms of error functions. For example, given a fluorescent emitter located at $\theta = (u_0, v_0)$, we have that

$$\int O(u) du = \frac{1}{2} \left(\operatorname{erf} \left(\frac{u_k + \frac{1}{2} - u_0}{\sqrt{2}\sigma} \right) - \operatorname{erf} \left(\frac{u_k - \frac{1}{2} - u_0}{\sqrt{2}\sigma} \right) \right) \quad (11)$$

where we have used the common definition $\operatorname{erf}(z) = \frac{2}{\sqrt{\pi}} \int_0^z e^{-t^2} dt$. Our generative model also incorporates a normally distributed white noise per pixel ζ with offset o and variance σ^2 . Ultimately, we have a Poisson component of the signal, which scales with N_0 and a Gaussian component, which does not.

Consider,

$$\zeta_k - o_k + \sigma_k^2 \sim \mathcal{N}(\sigma_k^2, \sigma_k^2) \approx \text{Poisson}(\sigma_k^2) \quad (12)$$

Since $\mathbf{x}_k = \mathbf{s}_k + \zeta_k$, we transform $\mathbf{x}'_k = \mathbf{x}_k - o_k + \sigma_k^2$, which is distributed according to

Consider the factorization $p(\hat{\mathbf{y}}|\mathbf{x}, \mathbf{y})p(\mathbf{x}|\mathbf{y})p(\mathbf{y}) = p(\mathbf{x}|\mathbf{y}, \hat{\mathbf{y}})p(\mathbf{y}|\hat{\mathbf{y}})p(\hat{\mathbf{y}})$. Given that \mathbf{x} is conditionally independent of $\hat{\mathbf{y}}$, we find

$$p_{\Psi}(\hat{\mathbf{y}}|\mathbf{x}, \mathbf{y}) = p(\mathbf{y}|\hat{\mathbf{y}})$$